Journal of Nondestructive Evaluation (2018) 37:70
https://doi.org/10.1007/s10921-018-0520-2

Study of the Choice of Excitation Frequency for Sub Surface Defect Detection in Electrically Thick Conducting Specimen Using Eddy Current Testing

Mahesh Raja Perumal[1] · **Krishnan Balasubramaniam**[2] · **Kavitha Arunachalam**[1]

Received: 21 September 2017 / Accepted: 28 July 2018 / Published online: 4 September 2018

Abstract
Understanding the scope and limitations of non-destructive testing procedure is essential for selecting the appropriate test parameters for material inspection. This paper presents the scope of material (δ_s) and probe dependent (δ_t) penetration depths for determining the optimal test frequency (f_{opt}) for detection of sub surface defects in electrically thick conducting specimens. Numerical modelling is carried out for a pancake coil above an electrically thick aluminium plate, $t/\delta_t > 1$, to study the influence of the EC probe and defect location (t_{df}) on the test frequency for near and deep sub surface defects. The study concludes that the optimal test frequency, f_{opt} for detection of deep sub surface defects ($t_{df}/t \approx 1$) is determined by the probe dependent skin depth, δ_t, and the plate thickness is related to f_{opt} by, $t \propto 1/\sqrt{f_{opt}}$. The numerical observations were experimentally validated for machined sub surface notches on a 10 mm thick (t) aluminium plate.

Keywords Conducting specimen · Eddy current testing · Sub surface defect · Thick plate

1 Introduction

Eddy current testing (ECT) is one of the most widely used non-destructive testing (NDT) method for flaw detection and characterisation, thickness measurement, and estimating internal structural changes in electrically conducting materials and components [1]. The sensitivity of the eddy current (EC) coil is largely influenced by the coil parameters namely, number of turns, spacing between the windings, dimensional aspect ratio of the coil and the internal ferrite core length [2]. Due to the limited penetration of the EC governed by the skin depth (δ_s) effect, ECT is commonly used for inspecting defects and corrosion in few mm thick metallic structures and components [3–5]. Besides defect detection, ECT is proposed for bulk material inspection such as evaluating the equi bi-axial compressive stress in non-ferromagnetic materials [6], evaluating the extent of carburization in reformer tubes [7], and assessing the weld quality of spot resistance welding technique [8].

In electrically thick conducting specimens, the induced EC and the magnetic field variation in the specimens are primarily confined to the material surface and near sub surface regions. Thus, increasing the penetration depth by lowering the excitation frequency lowers the signal to noise ratio as the voltage induced in the sensing coil is proportional to the rate of change of the magnetic field. An alternate to the traditional single or multi frequency excitation coils that are operated either in absolute or differential mode is the pulsed eddy current (PEC) testing. The broad frequency spectrum allows the detection of surface and near surface defects in PEC testing [9, 10]. Due to the skin depth limitation of the pickup coil [11, 12], detection of deep sub surface defects in electrically thick specimens remains a challenge. Thus, there is an increased interest in using sensitive magnetic field sensors such as Giant Magneto Resistor (GMR) [13, 14], Hall effect sensor [15] and Superconducting Quantum Interference Device (SQUID) sensor [16] for deep sub surface defects.

An electrically thick conducting specimen of thickness, t satisfies the criterion, $t/\delta_s > 1$. Thus, the specimen thickness is several times the standard penetration depth. As the

✉ Kavitha Arunachalam
akavitha@iitm.ac.in

[1] Electromagnetic Research Laboratory, Department of Engineering Design, Indian Institute of Technology Madras, Chennai, Tamil Nadu 600036, India

[2] Department of Mechanical Engineering, Centre for Non-Destructive Evaluation (CNDE), Indian Institute of Technology Madras, Chennai, Tamil Nadu 600036, India

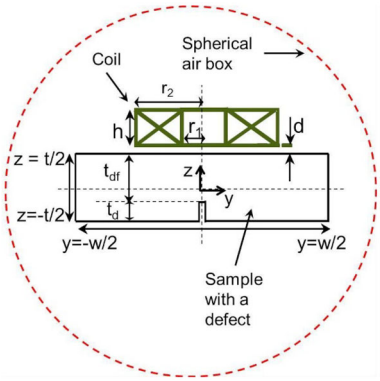

Fig. 1 Cross sectional view of the numerical model

frequency dependent skin depth, δ_s obtained for plane wave excitation of an infinitely extended plate is greater than the probe dependent skin depth, δ_t [17], the criterion, $t/\delta_t > 1$ also defines an electrically thick conducting specimen. In electrically thick conducting specimens, the sensitivity of the EC probe for sub surface and deep sub surface defects vary with the defect location. Thus, it is important to understand the role of probe dependent penetration depth for defect detection in electrically thick conducting specimens. In this paper, we present 3D numerical analysis of ECT to understand the scope and limitations of δ_s and δ_t for sub surface and deep sub surface defect detection using a pancake coil in electrically thick conducting specimen. Thus, simulations are reported for centrally located defect in a large plate and the influence of lift-off variation on probe impedance is not covered. The paper is organised as follows: Sect. 2 presents the 3D numerical model and study of the influence of probe size on optimal excitation frequency for varying plate dimensions, and the influence of defect location on the optimal test frequency for detection. Section 3 presents the experimental verification of the numerical analysis on an electrically thick aluminium plate with machined defects of varying depths. Section 4 concludes this work.

2 3D Numerical Model

A 3D model of a pancake coil above an electrically thick conducting specimen was developed in COMSOL® Multiphysics, a Finite Element Method (FEM) based simulation software to calculate the coil impedance for varying excitation frequency, plate dimensions and defect depth. Figure 1a shows the zoomed in 2D cross section of the 3D computational domain implemented in COMSOL. A pancake coil of height, h with inner and outer radii, r_1 and r_2 respectively placed at a distance, d above a planar electrically thick conducting specimen of dimensions, $l \times w \times t$ was modelled. The numerical model solves the governing equation,

$$\nabla^2 \vec{A} = -\mu_0 \vec{J}_s + \mu_0 \sigma \left(\frac{\partial \vec{A}}{\partial t} \right), \tag{1}$$

where $\vec{A}$ is the magnetic vector potential, $\vec{J}_s$ is the source current density maintained by the coil at the excitation frequency, μ_0 and σ are the magnetic permeability and bulk electrical conductivity of the material respectively.

The computational domain was enclosed by a spherical air domain with magnetic insulation boundary condition, $\hat{n} \times \vec{A} = 0$, on the external boundary surface. Coil excitation was specified at a single frequency using surface source current density, $\vec{J}_s$ given by, $(NI/A_c)\vec{e}_{coil}$, where I is the current flowing through the coil, A_c is the wire cross sectional area, N is the number of turns, and $\vec{e}_{coil}$ is the current direction in the coil. The computation domain was discretised into tetrahedral elements and numerical solution was obtained using Flexible Generalised Minimal Residual (FGMRES) iterative solver. The best practices for solving 2D/3D EC problems in COMOSL were implemented in the numerical simulations for model convergence [18]. With the knowledge of the magnetic vector potential ($\vec{A}$), the electric and magnetic fields were computed everywhere in the computational domain. The impressed current, $I(\omega)$ and voltage induced in the coil, $V_{ind}(\omega)$ calculated from the electric field were used to calculate the coil impedance,

$$Z(\omega) = \frac{I(\omega) R_{DC} - V_{ind}(\omega)}{I(\omega)}, \tag{2}$$

where R_{DC} is the DC coil resistance and $\omega = 2\pi f$ is the angular frequency. Simulation results of the EC numerical model implemented in COMSOL were validated with benchmark problems with good agreement between model and measurements [18].

3 Numerical Analysis

Numerical simulations were carried out for a defect free 10 mm thick (t) aluminium plate with electrical conductivity, $\sigma = 30$ MS/m, magnetic permeability, μ_0, plate dimensions, 100 mm × 100 mm × 10 mm ($l = 100$ mm, $w = 100$ mm), coil parameters, $r_1 = 1.5$ mm, $h = 3$ mm and $N = 530$, and 0.5 mm lift off (d). A sinusoidal coil current of 20 mA (I) was fed to the coil with wire gauge of 38.

3.1 Influence of Coil Size on Test Frequency

The coil outer radius was swept from 6 to 9 mm in steps of 0.5 mm. The sweep range for r_2 was selected such that the coil diameter ($D_2 = 2\, r_2$) is less than the sample lateral dimensions ($l \times w$) to avoid plate edge effects in the simulations. Figure 2 shows the zoomed in surface mesh in the coil

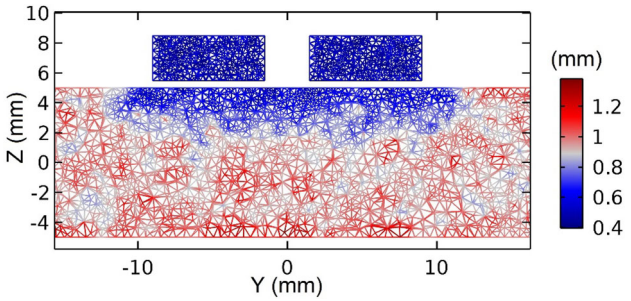

Fig. 2 Surface plot of the finite element mesh in coil and specimen domains (zoomed view)

and sample domains. A non-uniform mesh with higher mesh density in the coil domain and plate volume beneath the coil was selected to capture the fast decaying induced EC and the secondary magnetic field with reduced computational overheads. The skin depth at 100 Hz is approximately equal to the plate thickness i.e., $t \approx \delta_s$. Thus, coil excitation frequency was swept from 100 to 1500 Hz so that t/δ_s varied over 1–3 satisfying the criterion for an electrically thick conducting specimen. Numerical simulations were carried out for varying r_2 and f, and the induced current density, $\vec{J}_e$ calculated at the plate bottom defined at ($x = 0$, $y = r_2$, $z = -t/2$) was used to study the influence of coil size on the excitation frequency for ECT.

Figure 3a shows the norm of the eddy current density, $\left|\vec{J}_e\right|$ induced at the plate bottom for 12 mm and 18 mm coil outer diameter (OD) over 100–1500 Hz i.e., f corresponding to 1–3 δ_s. It can be observed that the maximum eddy current density ($\left|\vec{J}_e\right|$) is induced at the plate bottom for larger coil OD (18 mm), and the coil excitation frequency corresponding to the maximum eddy current density ($\left|\vec{J}_e\right|$) decreases with increase in coil OD, $\boldsymbol{D}_2$. The optimal test frequency, f_{opt} corresponding to the maximum $\left|\vec{J}_e\right|$ is 450 Hz and 550 Hz for 18 mm and 12 mm coil ODs respectively. Figure 3a clearly indicates that there exists a probe dependent optimal test frequency (f_{opt}) below which even though the skin depth increases, the induced EC at the plate bottom weakens. Figure 3b shows the induced current density in logarithmic scale at 350 Hz corresponding to t/δ_s of 2 along the specimen depth indicated by cutline AB defined at ($x = 0$, $y = r_2$). In Fig. 3b, the true penetration depth, δ_t calculated at 350 Hz for $\boldsymbol{D}_2$ of 18 mm and 12 mm is 3.5 mm and 2.8 mm respectively. This value is far less than the standard skin depth, δ_s of 4.9 mm at 350 Hz. It can also be observed from Fig. 3b that at $z = \delta_s$, $\left|\vec{J}_e\right|$ is far less than 37%. As the EC current density is more for the 18 mm coil OD than 12 mm coil OD, pancake coil with $r_1 = 1.5$ mm, $r_2 = 9$ mm, $h = 3$ mm, and $N = 530$ turns was selected to study the influence of plate thickness, t and width, w on f_{opt} and δ_t.

3.2 Influence of Plate Dimensions on Excitation Frequency

Numerical simulations of defect free aluminium specimen were carried out for 10 mm thick plate of 100 mm (l) length and varying plate width (w) to study the influence of plate edges on the test frequency. Simulations were carried out for a pancake EC probe of 18 mm coil OD and 0.5 mm lift off (d). Figure 4 shows the normalised eddy current density

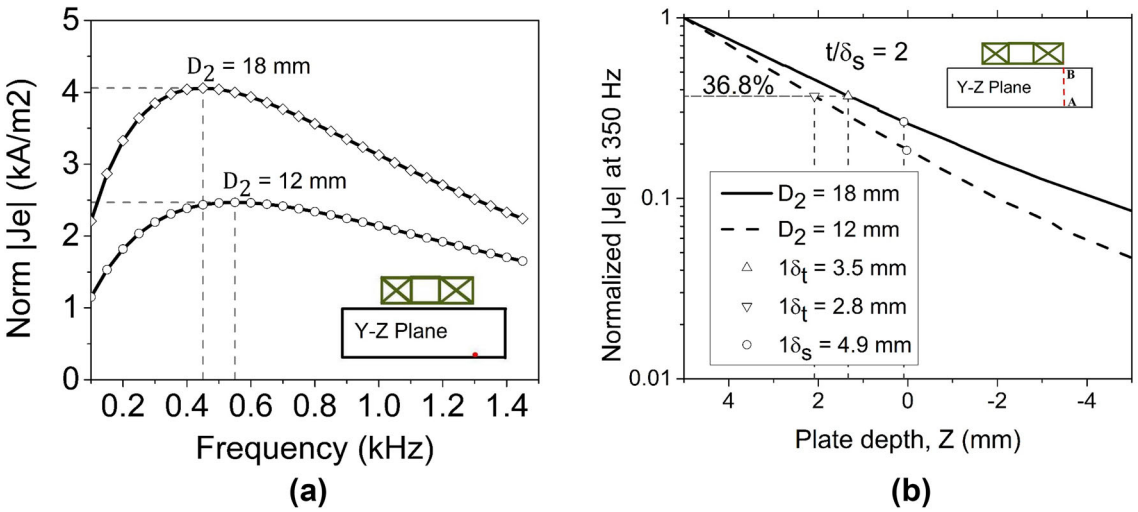

Fig. 3 **a** Eddy current density at plate bottom defined at ($x = 0$, $y = r_2$, $z = -t/2$) for 18 mm and 12 mm coil ODs; **b** normalized eddy current density in logarithmic scale for 18 mm and 12 mm coil ODs at 350 Hz ($t = 2\,\delta_s$) along the specimen depth indicated by cutline AB shown in the figure inset

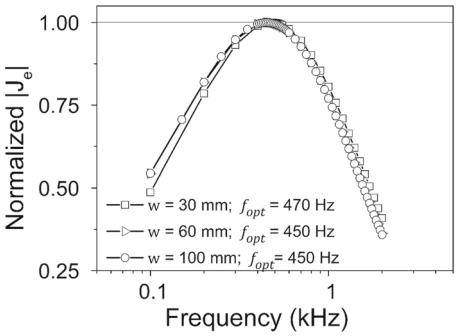

Fig. 4 Influence of plate width on coil excitation frequency (l = 100 mm). Normalized current density at the bottom of a 10 mm thick plate

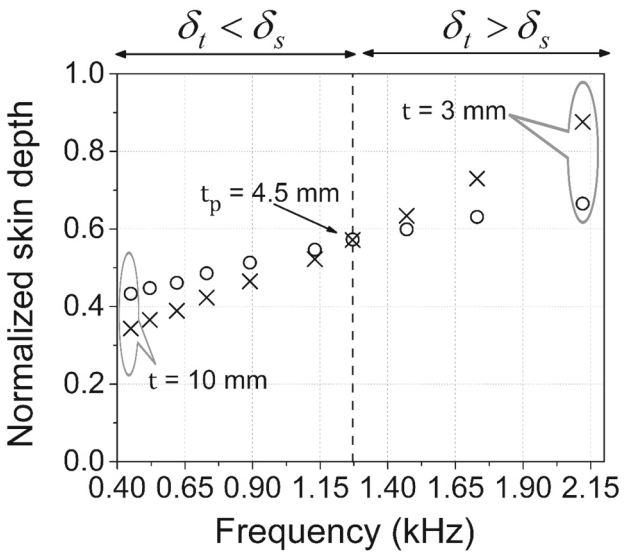

Fig. 6 Normalized skin depths, δ_s/t and δ_t/t at the optimal test frequency (f_{opt}) in electrically thick conducting plate. Plate length and width are 100 mm each

calculated at the plate bottom for varying plate widths (w : 30–100 mm). For $w > 3\ D_2$, the optimal test frequency, f_{opt} approached 450 Hz which corresponds to f_{opt} for a large specimen without plate edge effect i.e., ($l \times w$) of 100 mm × 100 mm. From Fig. 4 it can be concluded that the plate width does not significantly influence the optimal test frequency, f_{opt} for a finite size plate.

Simulations were also carried out for varying plate thickness (t) of a wide specimen (l = 100 mm, w = 100 mm) excited by a pancake coil of 18 mm coil OD. Figure 5a shows the normalised EC density induced at the plate bottom for varying plate thickness. In Fig. 5a, as plate thickness increased, the optimum frequency (f_{opt}) corresponding to the maximum $\left|\vec{J}_e\right|$ at the plate bottom decreased monotonically. The induced EC strength at the plate bottom also decreased with increase in plate thickness, t as shown in Fig. 5b. It should be noted that the plate thicknesses in Fig. 5 satisfy the criterion, $t > \delta_s$, where δ_s is computed at the f_{opt} determined from FEM simulations for the respective thickness, t. From Fig. 5b, it can be observed that plate thickness, $t \propto 1/\sqrt{f_{opt}}$ for an electrically thick conducting plate. The simulation results are in agreement with the empirical relationship reported by Nagendran et al. for deep sub surface defects [16] Furthermore, the simulation results in Figs. 4 and 5 indicate that for a given coil design, plate thickness, t significantly influences the optimal test frequency, f_{opt} than the plate lateral dimensions ($l \times w$).

3.3 Influence of Plate Thickness on Skin Depth

Figure 6 shows the normalized true (δ_t/t) and standard (δ_s/t) skin depths calculated at f_{opt} for varying plate thickness, t : [3, 10] mm with lateral plate dimensions, l =

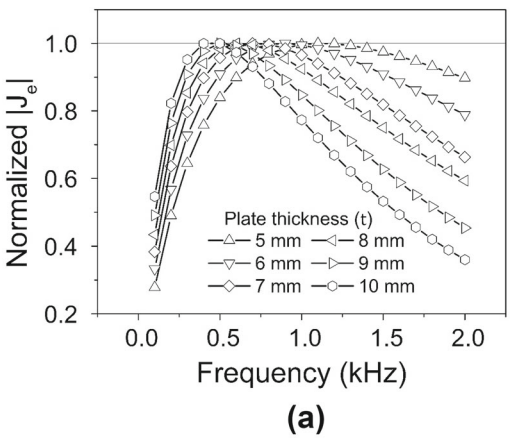

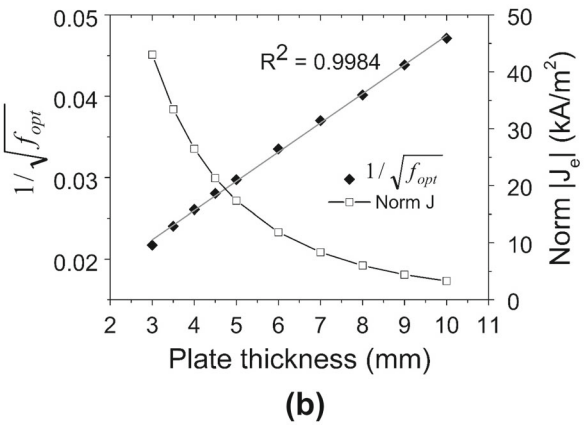

Fig. 5 Influence of plate thickness on coil excitation frequency (l = 100 mm, w = 100 mm). **a** Normalized current density at plate bottom, **b** dependence of f_{opt} and surface current density on plate thickness, t

100 mm and $w = 100$ mm. In Fig. 6, the material dependent standard penetration depth, δ_s is computed at the f_{opt} determined from FEM simulations for the respective thickness, t. From Fig. 6, it can be noted that the graph can be divided into two regions: region I, where standard skin depth is more than the true skin depth ($\delta_t < \delta_s$), and region II, where $\delta_t > \delta_s$. In Fig. 6, the standard skin depth at f_{opt} computed based on plane wave theory, and true skin depth numerically calculated based on the coil design at f_{opt} are equal for $t = 4.5$ mm (t_p). For $t < t_p$ (region II), the induced EC density at f_{opt} shown in Fig. 5b attenuates slower than the exponential decay rate for a plane wave source. Thus, $\delta_t > \delta_s$ in region II. As plate thickness increased beyond t_p (region I), the EC density induced by the pancake coil at f_{opt} decayed faster than the plane wave source. Thus, deep sub surface defect detection in electrically thick plates ($t/\delta_t > 1$) must be based on the probe dependent penetration depth, δ_t [19], and the scope of δ_s for defect detection must be limited to thin plates which lie in region II. In Fig. 6, δ_t/t varies over 0.876–0.343 for plate thickness, t : [3, 10] mm. The ratio, δ_t/t of 1/3 corresponds to 5% of $|\vec{J_e}|$ at the plate bottom ($z = -t/2$) which is relatively weak to induce a measurable change in the coil impedance. Thus, sensitivity of the EC coil for deep sub surface defect detection in electrically thick plate ($t/\delta_t > 1$) decreases with increase in t. As a result, defect detection using an absolute coil can only be improved by increasing either the coil diameter, D_2 or excitation current, I. Increasing D_2 increases $\left|\vec{J}_e^{max}\right|$ at the plate bottom, lowers f_{opt} and reduces the spatial resolution of EC coil for defect localization. Increasing coil current, I leads to coil heating which increases the ohmic loss and causes measurement instability. To avoid these issues, deep sub surface defect detection is typically carried out using either a sensitive secondary coil [20] or GMR as the pick-up sensor [21].

3.4 Influence of Defect Depth on Coil Impedance

Numerical simulations were carried out to study the influence of defect depth, t_{df} on coil impedance over 100–2000 Hz covering f_{opt}. Two dimensional notch of length, 100 mm, breadth, 2 mm and height, t_d was introduced at the bottom of a 100 × 100 × 10 mm^3 plate. Figure 7 shows the change in coil impedance, $\Delta Z = \Delta R + j\Delta X$ for varying defect depth in the 10 mm thick plate, where $\Delta R = R_D - R_{ND}$, $\Delta X = X_D - X_{ND}$, R_D and R_{ND} are coil resistances calculated in the presence and absence of the notch respectively, and X_D and X_{ND} are coil reactances calculated in the presence and absence of the notch respectively. The resistance and inductance values of the simulated coil are 37 Ω and 2.4 mH respectively. The coil location above the specimen with 2D notch is illustrated in Fig. 7. From Fig. 7,

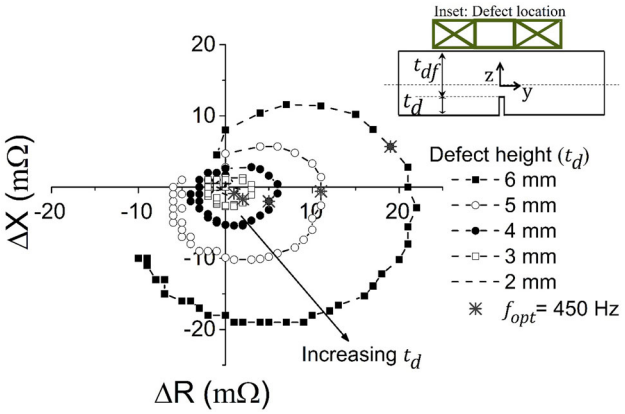

Fig. 7 Simulated change in coil impedance, $\Delta Z = \Delta R + j\Delta X$ for varying defect height, t_d over 100–2000 Hz. Inset: Coil location simulated for impedance calculation

Table 1 Coil impedance, ΔZ at f_{opt} for a 2 mm wide 2D notch at the bottom of an electrically thick aluminium plate ($t/\delta_t = 2.9$, $\delta_t = 3.4$ mm, $f_{opt} = 450$ Hz) for varying notch height, t_d. Change in the impedance magnitude ($|\Delta Z|$), and phase $\angle(\Delta Z)$ were calculated with reference to the coil impedance above a defect free plate

Sl. no.	Notch height, t_d (mm)	$\lvert \Delta \mathbf{Z} \rvert$ at f_{opt} (m **Ω**)	Phase change, $\angle(\Delta \mathbf{Z})$ at f_{opt} (°)
1	2	1.35	−41.99
2	3	2.62	−40.36
3	4	5.39	−21.80
4	5	11.02	−3.12
5	6	19.84	16.70

it can be observed that the coil impedance, Z at f_{opt} varies with notch height, and the phase change rotates to the 1st quadrant as the notch moves closer to the coil. Table 1 lists the change in coil impedance, ΔZ for varying notch height, t_d in an electrically thick plate ($t/\delta_t = 2.9$, $\delta_t = 3.4$ mm, $f_{opt} = 450$ Hz). From Fig. 7 and Table 1, it can be concluded that the change in coil impedance at f_{opt} can be used to detect and also estimate the location of the defect.

4 Experimental Validation

4.1 Test Specimens and Measurement Set Up

Two aluminium plates of 10 mm thickness were used as test specimens. Specimen A is a calibration block of dimension 100 × 30 × 10 mm^3 made of 2024-T3 aluminium alloy with a centrally located 2D notch and specimen B is a rectangular aluminium plate of dimension 400 × 100 × 10 mm^3 containing three equally spaced 2D notches located 120 mm apart. The dimensions of the notches fabricated using Electro

Table 2 Dimenions of the 2D EDM notches in aluminium specimens

Sample	EDM notch (sample)	Length (mm)	Breadth (mm)	Height, t_d (mm)	Defect depth from surface, t_{df} (mm)
Specimen A	N1	30	0.5	1.5	8.5
Specimen B	N2	100	2	2	8
	N3	100	2	3	7
	N4	100	2	6	4

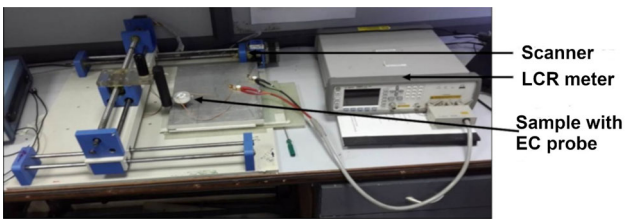

Fig. 8 ECT experimental set up

Discharge Machining (EDM) are summarized in Table 2. A pancake coil with $r_1 = 1.5$ mm, $r_2 = 9$ mm and $h = 3$ mm was fabricated using a 38 gauge copper wire and characterised using a LCR meter (E4980A, Agilent Technologies USA). The coil inductance and resistance values were measured as 2.72 mH and 25 Ω respectively. Figure 8 shows the experimental set up for ECT.

The impedance of the EC probe was measured using a LCR meter as the probe was scanned in steps of 1 mm with the help of a XY scanner controlled using LabVIEW® programming interface. The coil impedance measured by the LCR meter was logged at excitation frequencies in the neighbourhood of the optimal test frequency, f_{opt} calculated in Sect. 3.1. The coil lift-off and current was maintained as 0.5 mm and 20 mA respectively. The probe impedance above the defect free region, Z_{ND} was taken as the reference to calculate the change in coil impedance, $\Delta Z_n = \Delta R_n + j\Delta X_n$, at the nth scan position, where $\Delta R_n = R_n - R_{ND}$, $\Delta X_n = X_n - X_{ND}$, and R_n and X_n are the coil resistance and reactance at the nth scan position respectively.

4.2 Measurements and Data Analysis

Figure 9 shows the change in the coil impedance as the probe was scanned over specimen A with a deep sub surface notch (N1). Measurements indicate maximum impedance change at 450 Hz which is close to the optimal test frequency, f_{opt} (470 Hz) based on the true penetration depth, δ_t for the 30 mm wide specimen (Fig. 4a). The change in coil impedance for notch N1 at 450 Hz was measured as 1.60 mΩ ∠ −48.07 °

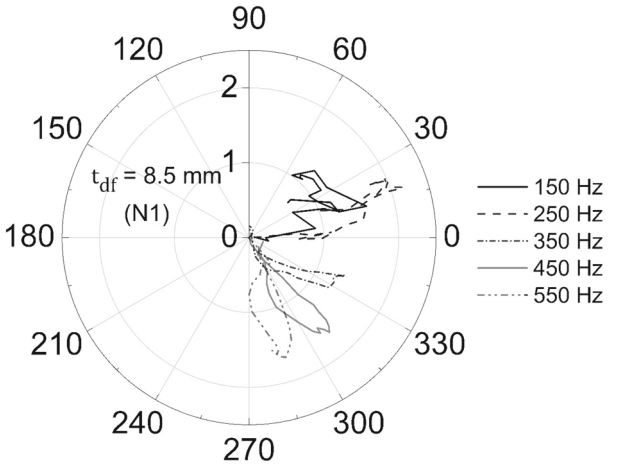

Fig. 9 Change in coil impedance for the deep sub surface notch, N1 (t_{df} = 8.5 mm, t = 10 mm) specimen A

with phase change close to −45°. At frequencies below f_{opt}, though the test frequency satisfy the criteria, $t/\delta_s < 3$, the coil response to deep sub surface defect at 150 Hz and 250 Hz is poor and noisy than at f_{opt}. At frequencies above f_{opt}, EC strength decreases due to decrease in probe penetration depth.

Figure 10 shows the change in coil impedance for specimen B as the EC probe was moved above the deep sub surface notches, N2 and N3 with defect location, $t_{df} > t/2$. The change in coil impedance at f_{opt} was measured as 5 mΩ ∠ −38.81° and 7.93 mΩ ∠ −34° for N2 and N3 notches respectively. As the defect depth from the plate surface (t_{df}) decreased, the phase change at f_{opt} moved away from −45° as observed in the simulations (Fig. 7, Table 1). Furthermore, due to the close proximity of the sub surface defect, the change in coil impedance is more for N3 than N2.

Figure 11 shows the change in coil impedance for the near sub surface notch, N4 located 4 mm from the plate surface i.e., $t_{df} < t/2$. Figure 11 shows the measurements at the test frequencies used for the deep sub surface notches, N2 and N3 shown in Fig. 10. The rotation of the impedance plane trajectory in Fig. 11 confirms that the impedance change is due to the defect. The phase change at f_{opt}(450 Hz) is + 19° (1st quadrant) indicating that the defect is a near surface defect. Thus, the experimental observation is in agreement with the simulations (Fig. 7, Table 1).

5 Conclusion

Unlike a plane wave source, the true penetration depth of an EC test coil depends on the material property as well as the coil dimensions. Furthermore, the magnetic field induced by a finite size coil approaches the field induced by a plane wave source as the coil becomes infinitely large. Thus, a

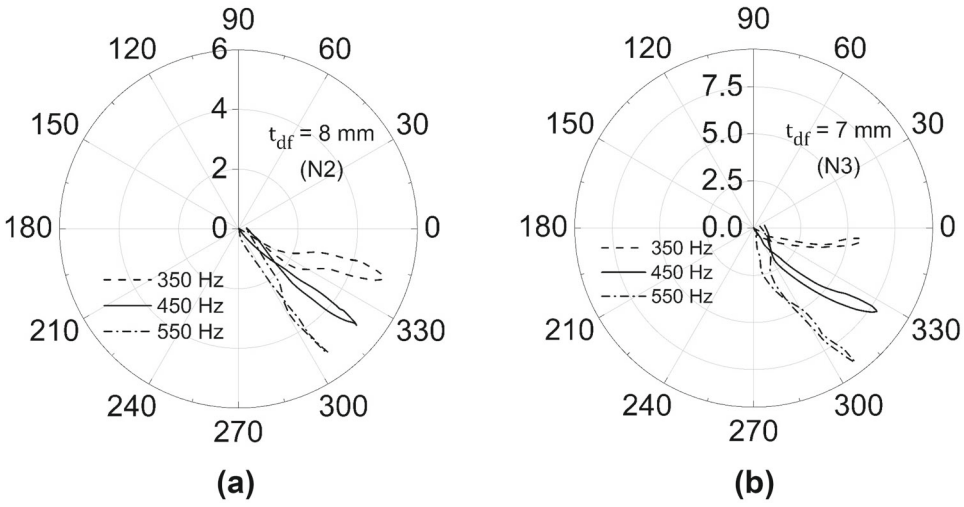

Fig. 10 Change in coil impedance for deep sub surface 2D notches. **a** t_{df} = 8 mm (N2), and **b** t_{df} = 7 mm (N3) in specimen B

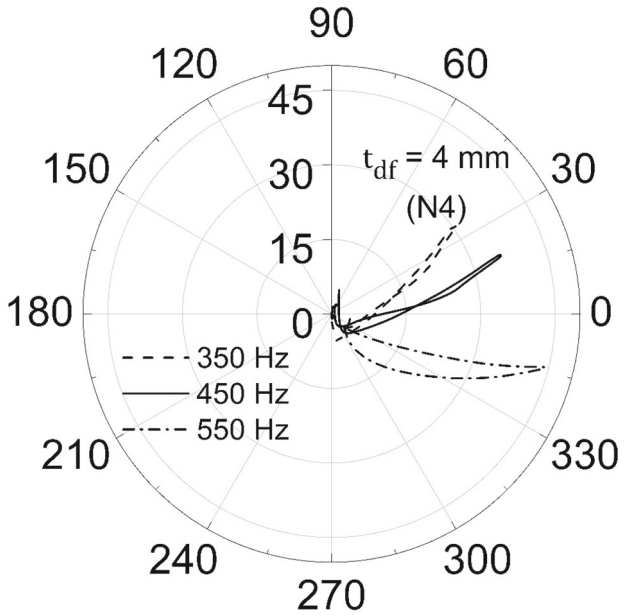

Fig. 11 Change in coil impedance for the sub surface 2D notch, N4 in specimen B. Impedance plane trajectory of the EC probe in the neighbourhood of FEM based f_{opt} of 450 Hz

larger test coil induced more EC in the specimen. As a result, the true penetration achieved by a finite size coil, δ_t is lower than the standard penetration depth, δ_s. 3D FEM simulations presented here clearly indicate the importance of the true (δ_t) penetration depth of a test coil for sub surface defect detection in electrically thick conducting specimens using ECT. The optimum test frequency, f_{opt} for deep sub surface defect detection in electrically thick specimens is given by δ_t which is primarily determined by the outer diameter of the EC probe and not the material dependent standard penetration depth, δ_s. Thus, the scope of standard penetration depth, δ_s for determining the test frequency is applicable for inspection of thin plates ($t/\delta_s < 1$). As the defect location from the plate surface decreases, the change in the phase of the complex coil impedance, $\angle\Delta Z$ at f_{opt} could be used to estimate the defect location. The numerical findings were experimentally verified on electrically thick aluminium plates for the EC probe dimensions studied in the FEM simulations. It is shown that the plate thickness, $t \propto 1/\sqrt{f_{opt}}$, and defect depth ($t_{df}$) can be estimated from $\angle\Delta Z$ measured at f_{opt}. The close agreement between simulations and measurements indicate that the proposed approach could be used for selecting EC probe and the optimal test frequency for defect detection in electrically thick conducting specimens.

Acknowledgements The authors thank Prof. Srinivas Veeturi, Department of Physics, Indian Institute of Technology Madras for access to the coil winding facility.

References

1. Blitz, J.: Electrical and magnetic methods of nondestructive testing. In: Hilger, A. Bristol, Philadelphia (1991)
2. Capobianco, T.E., Splett, J.D., Iyer, H.K.: Eddy current probe sensitivity as a function of coil construction parameters. Res. Nondestr. Eval. **2**(3), 169–186 (1990). https://doi.org/10.1007/bf01606356
3. Bouchala, T., Abdelhadi, B., Benoudjit, A.: Fast analytical modeling of eddy current non-destructive testing of magnetic material. J. Nondestr. Eval. **32**(3), 294–299 (2013). https://doi.org/10.1007/s10921-013-0182-z
4. Bouchala, T., Abdelhadi, B., Benoudjit, A.: Novel coupled electric field method for defect characterization in eddy current non-destructive testing systems. J. Nondestr. Eval. (2013). https://doi.org/10.1007/s10921-013-0197-5
5. Kim, J., Le, M., Lee, J., Hwang, Y.H.: Eddy current testing and evaluation of far-side corrosion around rivet in jet-engine intake of aging supersonic aircraft. J. Nondestr. Eval. **33**(4), 471–480 (2014). https://doi.org/10.1007/s10921-014-0242-z
6. Sekine, Y., Soyama, H.: Evaluation of equibiaxial compressive stress introduced into austenitic stainless steel using an eddy cur-

rent method. J. Nondestr. Eval. **31**(2), 99–107 (2011). https://doi.org/10.1007/s10921-011-0125-5
7. Hasegawa, K., Oikawa, T., Kasai, N.: Development of an eddy current inspection technique with surface magnetization to evaluate the carburization thickness of ethylene pyrolysis furnace tubes. J. Nondestr. Eval. **31**, 349–356 (2012). https://doi.org/10.1007/s10921-012-0146-8
8. Tsukada, K., Miyake, K., Harada, D., Sakai, K., Kiwa, T.: Magnetic nondestructive test for resistance spot welds using magnetic flux penetration and eddy current methods. J. Nondestr. Eval. **32**(3), 286–293 (2013). https://doi.org/10.1007/s10921-013-0181-0
9. Dolabdjian, C.P., Perez, L., Haan, V.O.D., Jong, P.A.D.: Performance of magnetic pulsed-eddy-current system using high dynamic and high linearity improved Giant Magneto-Resistance (GMR) Magnetometer. IEEE Sens. J. **6**(6), 1511–1517 (2006). https://doi.org/10.1109/JSEN.2006.883095
10. Arjun, V., Sasi, B., Rao, B.P.C., Mukhopadhyay, C.K., Jayakumar, T.: Optimisation of pulsed eddy current probe for detection of subsurface defects in stainless steel plates. Sens. Actuators, A **226**, 69–75 (2015). https://doi.org/10.1016/j.sna.2015.02.018
11. Joubert, P.Y., Vourc'h, E., Tassin, A., Le Diraison, Y.: Source separation techniques applied to the detection of subsurface defects in the eddy current NDT of aeronautical lap-joints. NDT E Int. **43**(7), 606–614 (2010). https://doi.org/10.1016/j.ndteint.2010.06.005
12. Soni, A.K., Sasi, B., Thirunavukkarasu, S., Rao, B.P.C.: Development of eddy current probe for detection of deep sub-surface defects. IETE Tech. Rev. **4602**, 1–10 (2015). https://doi.org/10.1080/02564602.2015.1113145
13. Sasi, B., Rao, B.P.C., Thirunavukkarasu, S., Jayakumar, T., Raj, B.: Eddy current-giant magneto-resistive (GMR) sensor for non-destructive detection of deep- surface defects. In: Procedings of National Symposim on Physics and Technology of Sensors, pp. 273–275 (2007)
14. Ye, C., Udpa, L., Udpa, S.: Optimization and validation of rotating current excitation with GMR array sensors for riveted structures inspection. Sensors **16**(9), 1512 (2016). https://doi.org/10.3390/s16091512
15. Park, D.-G., Angani, C.S., Rao, B.P.C., Vértesy, G., Lee, D.-H., Kim, K.-H.: Detection of the subsurface cracks in a stainless steel plate ssing pulsed eddy current. J. Nondestr. Eval. **32**(4), 350–353 (2013). https://doi.org/10.1007/s10921-013-0188-6
16. Nagendran, R., Thirumurugan, N., Chinnasamy, N., Janawadkar, M.P., Baskaran, R., Vaidhyanathan, L.S., Sundar, C.S.: Optimum eddy current excitation frequency for sub-surface defect detection in SQUID based non-destructive evaluation. NDT E Int. **43**, 713–717 (2010). https://doi.org/10.1016/j.ndteint.2010.08.003
17. Kundu, T.: Ultrasonic and Electromagnetic NDE for Structure and Material Characterization: Engineering and Biomedical Applications. CRC Press, Boca Raton (2012)
18. Theodoulidis, T.P., Martinos, J., Poulakis, N.: Numerical results for the WFNDEC 2012 eddy current benchmark problem. AIP Conf. Proc. **1511**(1825), 1825–1830 (2013). https://doi.org/10.1063/1.4789262
19. Mottl, Z.: The quantitative relations between true and standard depth of penetration for air-cored probe coils in eddy current testing. Ndt E Int. **23**(1), 11–18 (1990). https://doi.org/10.1016/0963-8695(90)90708-Q
20. Chady, T., Enokizono, M., Sikora, R.: Crack detection and recognition using an eddy current differential probe. IEEE Trans. Magn. **35**(3), 1849–1852 (1999). https://doi.org/10.1109/20.767393
21. Hamia, R., Cordier, C., Dolabdjian, C.: Eddy-current non-destructive testing system for the determination of crack orientation. NDT E Int. **61**, 24–28 (2014). https://doi.org/10.1016/j.ndteint.2013.09.005